The Dynamics of Boundary Layer Jets within the Tropical Cyclone Core. Part II: Nonlinear Enhancement

JEFF KEPERT

Bureau of Meteorology Research Centre, Melbourne, Victoria, Australia

YUQING WANG

School of Ocean and Earth Science and Technology, University of Hawaii at Manoa, Honolulu, Hawaii

(Manuscript received 5 June 2000, in final form 16 November 2000)

ABSTRACT

Observations of wind profiles within the tropical cyclone boundary layer until recently have been quite rare. However, the recent spate of observations from the GPS dropsonde have confirmed that a low-level wind speed maximum is a common feature of the tropical cyclone boundary layer. In Part I, a mechanism for producing such a maximum was proposed, whereby strong inward advection of angular momentum generates the supergradient flow. The processes that maintain the necessary inflow against the outward acceleration due to gradient wind imbalance were identified as being (i) vertical diffusion, (ii) vertical advection, and (iii) horizontal advection, and a linear analytical model of the boundary layer flow in a translating tropical cyclone was presented and used to diagnose the properties of the jet and the near-surface flow. A significant shortcoming was that the jet was too weak, which was argued to be due to the neglect of vertical advection. Here, a high-resolution, dry, hydrostatic, numerical model using the full primitive equations and driven by an imposed pressure gradient representative of a tropical cyclone is presented. It relaxes the constraint of linearity from Part I, includes the full advection terms, and produces a markedly stronger jet, more consistent with the observations. It is shown that the vertical advection of inflow is of major importance in jet dynamics, and that its neglect was the main reason that the linear model produced too weak a jet.

It is shown that the jet in a stationary storm is between 10% and 25% supergradient, depending on the particular characteristics of the storm. The height scale $(2K/I)^{1/2}$, where K is the turbulent diffusivity and I the inertial stability, obtained in Part I, is shown to fit the numerical model results well. This is typically several hundreds of meters in the cyclone core, and increases with radius. In the case of a moving Northern Hemisphere storm, it is found that the jet is most supergradient—several times stronger than in a stationary storm—at the eyewall to the left and front of the storm, as well as extending into a significant area around to the left of the storm. It is, however, much less marked to the right, where the strongest winds are found. This asymmetry is in good agreement with that found in Part I, and is dominated by the wavenumber 1 response forced by the asymmetric friction.

The factor for reducing upper winds to a near-surface equivalent, which is frequently used in operational work, is shown to have a substantial spatial variability. Larger values are found near the eye, due to the symmetric component of the solution. There is also an overall increase from right to left of the storm in the Northern Hemisphere, again consistent with the results in Part I.

1. Introduction

Low-level wind maxima have been frequently observed in the boundary layer of tropical cyclones. Kepert (2001, henceforth Part I) describes a physical mechanism for producing such a jet in which strong inward advection of angular momentum leads to supergradient flow. A key point was that some process must maintain the inflow against the outward acceleration due to gradient adjustment. In Part I, we presented a linear analytical model of the boundary layer of a moving tropical cyclone, and showed that vertical diffusion could maintain inflow in the presence of a weakly supergradient jet in the upper boundary layer. We argued that vertical advection, omitted in the linear model, would also help maintain the inflow and therefore allow a stronger jet, without substantially changing its height. Surface wind factors were also calculated, and found to increase toward the center of the storm. In a moving storm, it was found that the jet was stronger (more supergradient) on the left side of a Northern Hemisphere cyclone. There was also a broad left–right asymmetry in surface wind factor, with larger values on the weaker, left, side of the storm in the Northern Hemisphere. The two components

Corresponding author address: Dr. Jeff D. Kepert, Bureau of Meteorology Research Centre, GPO Box 1289K, Melbourne, Vic 3001, Australia.
E-mail: j.kepert@bom.gov.au

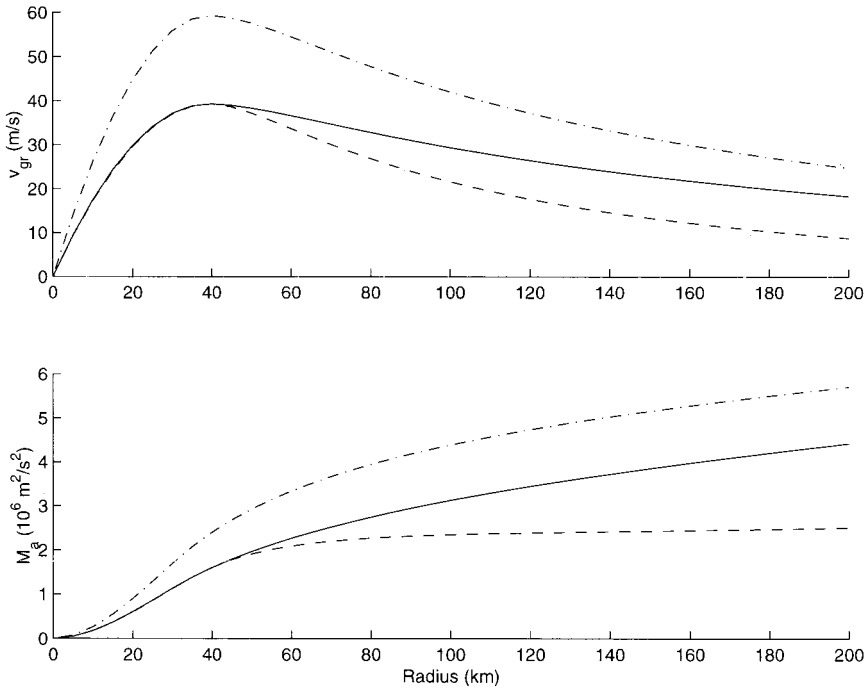

FIG. 1. Radial profiles of gradient wind speed (top) and absolute angular momentum (bottom) for the three stationary storms defined in Table 1: I solid, II dashed, and III dash–dotted.

that made up the motion-induced asymmetry were shown to be due to frictionally stalled inertia waves with azimuthal wavenumber 1.

Here we use a high-resolution, dry, hydrostatic numerical model with full primitive equations to significantly extend the results of Part I. In particular, we eliminate the linear constraint and quantify the importance of the nonlinear terms to jet development. We adopt a much more realistic representation of the turbulence, and show that the jet is not a consequence of frictional decoupling due to near-surface stabilization resulting from the cold near-surface conditions observed by Korolev et al. (1990), Black et al. (1993), and Cione et al. (2000). We also analyze in detail the boundary layer flow beneath an inertially neutral storm, a case that is outside the validity range of the linear model.

In section 2, we describe our high-resolution model of the tropical cyclone boundary layer. We then use this model to study stationary storms in section 3, and moving storms in section 4. Particular attention will be paid to the nonlinear terms and the relationship of the results to those in Part I. The final section contains further discussion and conclusions.

2. Model formulation

As in Part I, we regard the tropical cyclone boundary layer as the frictional response to some known, steady-state cyclone in the free atmosphere, which we prescribe. We choose specifically to ignore the influence that details of the boundary layer structure may have on the cyclone as a whole. While these clearly exist—for example, the pattern of boundary layer convergence will affect the distribution of convection and hence heating—the scope of this study is rather to explore just one side of what is undoubtedly a two-way interaction. We opt also not to attempt to resolve the effects of convection on the boundary layer, concentrating rather on larger scales. While studies (e.g., Powell 1990a,b; Barnes and Powell 1995) have shown significant modulation of boundary layer structure in the vicinity of rainbands, on scales comparable to the width of the band, we prefer to focus at present on building an understanding of the larger-scale features of the tropical cyclone boundary layer.

Accordingly, we opt for a shallow model domain (2.1 km in the simulations presented here), with the top boundary condition including a translating parametric pressure field intended to represent the remainder of the cyclone. A benefit of this approach is that it allows much higher vertical resolution in the boundary layer than is customary in numerical tropical cyclone simulation, as there is no need to waste grid levels on resolving the entire storm. In addition, the intensity, radial wind profile and movement of the storm, as well as the environmental flow, are easily and independently adjustable.

Consistent with our focus on the boundary layer as a response to the ''free atmosphere'' flow, our representation of that by a parametric pressure field, and our neglect of convection, we exclude moisture from the model. Had it been included, its sole role (apart from

that of passive tracer) would be a tiny contribution to the height variation of pressure, through the hydrostatic equation.

Tropical cyclones are known to support a variety of instabilities that may result in the formation of smaller-scale structures embedded in the flow. These transient features would complicate the analysis, without contributing to our understanding. Some are suppressed by our use of a prescribed fixed pressure field, but it is necessary to carefully choose this so that the barotropic instability noted by Schubert et al. (1999) is not supported. In the real atmosphere, we expect that the cyclone-scale boundary layer flow described here may be modulated by these smaller-scale features.

a. Governing equations

The boundary layer model is based on the three-dimensional nonlinear primitive equations of a dry, continuously stratified, hydrostatic, Boussinesq atmosphere. The terrain-following vertical coordinate $z^* = z_t(z - z_s)/(z_t - z_s)$, where $z_s(x, y)$ is the height of the lower boundary and z_t is the height of the model top, is used to allow for future landfall and orographic effect studies, although the lower boundary is treated as a smooth sea surface here. The governing equations[1] are

$$\frac{du}{dt} = fv - \theta\frac{\partial \pi}{\partial x} - g\left(1 - \frac{z^*}{z_t}\right)\frac{\partial z_s}{\partial x} + K_H\nabla^4 u + \left(\frac{z_t}{z_t - z_s}\right)^2\frac{\partial}{\partial z^*}\left(K_v\frac{\partial u}{\partial z^*}\right)$$

$$\frac{dv}{dt} = -fu - \theta\frac{\partial \pi}{\partial y} - g\left(1 - \frac{z^*}{z_t}\right)\frac{\partial z_s}{\partial y} + K_H\nabla^4 v + \left(\frac{z_t}{z_t - z_s}\right)^2\frac{\partial}{\partial z^*}\left(K_v\frac{\partial v}{\partial z^*}\right)$$

$$\frac{d\theta}{dt} = K_H\nabla^4\theta + \left(\frac{z_t}{z_t - z_s}\right)^2\frac{\partial}{\partial z^*}\left(K_h\frac{\partial \theta}{\partial z^*}\right)$$

$$\frac{\partial \pi}{\partial z^*} = -\left(1 - \frac{z_s}{z_t}\right)\frac{g}{\theta}$$

$$\frac{\partial u}{\partial x} + \frac{\partial v}{\partial y} + \frac{\partial w^*}{\partial z^*} = \frac{u}{z_t - z_s}\frac{\partial z_s}{\partial x} + \frac{v}{z_t - z_s}\frac{\partial z_s}{\partial y}, \quad (1)$$

where

$$\frac{d}{dt} = \frac{\partial}{\partial t} + u\frac{\partial}{\partial x} + v\frac{\partial}{\partial y} + w^*\frac{\partial}{\partial z^*}, \quad \text{and} \quad (2)$$

$$\pi = C_p\left(\frac{p}{p_0}\right)^{R/C_p} \quad (3)$$

is the Exner function with $p_0 = 1000$ hPa. The relationship between the vertical velocity w in Cartesian (x, y, z) coordinates and that in the terrain-following coordinates is given by

$$w = \left(1 - \frac{z_s}{z_t}\right)w^* + \left(1 - \frac{z^*}{z_t}\right)\left(u\frac{\partial z_s}{\partial x} + v\frac{\partial z_s}{\partial y}\right). \quad (4)$$

In these equations, u, v are wind components in the x and y directions, respectively; θ is the potential temperature; f the Coriolis parameter (evaluated at 15°N); p the pressure; C_p the specific heat capacity of dry air at constant pressure; and g the gravitational acceleration. The horizontal diffusion is handled following Smagorinsky et al. (1965), as modified by Grell et al. (1994) to enhance the damping of short waves, with the diffusion coefficient given by

$$K_H = \frac{1}{2}k^2\Delta^4|D|, \quad (5)$$

where $k = 0.4$ is the von Kármán constant, Δ is the horizontal grid spacing, and $|D|$ the total horizontal deformation. For the simulations presented here, this gives maximum values of $\Delta^2 K_H$ in the range $2–4 \times 10^3$ $m^2\ s^{-1}$ near the radius of maximum winds. Finally, K_v and K_h are the vertical turbulent exchange coefficients for momentum and heat, respectively. These latter variables are given by the turbulence closure scheme, which is the quasi-equilibrium E-l scheme of Galperin et al. (1988) [also known as the level 2¼ scheme in the Mellor–Yamada (1974) hierarchy], with improved realisability conditions after Helfand and LaBraga (1988) and Gerrity et al. (1994). Surface fluxes are handled by Monin–Obukhov similarity theory with over-sea roughness lengths according to Charnock (1955) as modified by Smith (1988) for momentum, and Liu et al. (1979) as modified by Fairall et al. (1995) for heat and moisture, while the sea surface temperature is held fixed and constant at 300 K.

b. Solution procedure

The governing equations are discretized and numerically integrated over an unstaggered grid in the horizontal and a staggered grid in the vertical. The model consists of 15 layers in the vertical from the surface to z_t, the top of the model, with the midpoints of the layers at $z^* = 22.5$, 75.0, 142.5, 225.0, 322.5, 435.0, 562.5, 705.0, 862.5, 1035.0, 1222.5, 1425.0, 1642.5, 1875.0, and 2122.5 m. Horizontal velocity, potential temperature, and Exner function are defined at these midpoints, with the vertical velocity w^* and turbulence variables

[1] The numerical model is formulated in Cartesian coordinates, while the linear model of Part I and the analysis of results to come are in cylindrical coordinates. Although u and v are used for the velocity components in both coordinate systems and there is thereby a risk of confusion, the context will always make it clear which is intended.

(including the turbulent kinetic energy, mixing length, and vertical diffusivities) on the interfaces. The horizontal mesh of the model consists of 151 by 151 grid points with a uniform grid spacing of 5 km.

A two-time-level, explicit time-split scheme similar to that used in Wang (1998) is used for the model time integration. The procedure consists of an advection stage followed by an adjustment stage, and then a physical process stage. The same time step of 24 s is used for all stages to reduce the time-split errors. The forward-in-time upstream advection scheme developed by Wang (1996) is adopted for the advection stage. This advection scheme has third-order accuracy for time-dependent and nonuniform flow, and possesses very weak dissipation, very small phase errors, and good shape-conserving properties.

The adjustment stage is accomplished by the forward–backward scheme with the Coriolis force term treated implicitly in order to dampen inertial oscillations. The horizontal pressure gradient at the top of the model is known exactly from the applied pressure field, and the small differences to this in the remainder of the model are calculated by integrating the horizontal gradient of the hydrostatic equation downwards from the upper boundary, using centered second-order differences for the horizontal temperature gradient. As the horizontal pressure gradient at any level is due almost entirely to the prescribed upper boundary condition, the use of a relatively low order of accuracy for the horizontal gradient is unimportant.

The vertical advection terms are calculated by a second-order, centered differencing scheme, with vertical motion diagnosed by integrating the continuity equation upward from the surface. Thus mass is allowed to enter or exit the top of the model as required by the local net horizontal convergence. The vertical diffusion is accomplished by a semi-implicit centered scheme with weight 1.5 on a future time step (Kalnay and Kanamitsu 1988). The horizontal diffusion is discretized via a centered second-order scheme for the space derivatives, and a forward time stepping scheme.

The initial condition was of uniform temperature at the sea surface temperature (300 K) and winds in gradient balance with the prescribed pressure field, except in the lowest level where they were reduced by 35%, primarily to ensure they remained within the validity range of the surface layer scheme. The model was run out for 24 h, by which time all fields had attained a steady state.

A translating coordinate system is used in which the lower boundary together with the mesh of the model is shifted so that the parameterized tropical cyclone is stationary in the model domain. This allows the use of a relatively small computational domain. The movement of the lower boundary and model mesh is achieved by adding a vector equal to the cyclone translation velocity to the horizontal advection flow.

The use of a time split integration scheme greatly facilitated the calculation of budgets, which were done by saving the model state after each successive physical process was calculated. These were transformed from Cartesian into cylindrical coordinates and the tendency due to each physical process calculated from successive saves.

c. Boundary conditions

The pressure field at the top of the model is prescribed using a slightly modified version of analytical profile of Holland (1980), translating with a prescribed velocity. A uniform pressure gradient to represent the large-scale boundary layer flow may be optionally added. In the calculations presented here, this is set equal to the cyclone translation. The Holland (1980) profile has a number of advantages, as discussed in Part I. A minor deficiency is that it has a reversed radial vorticity gradient within the radius of maximum winds (RMW) and therefore satisfies the necessary conditions for barotropic instability (Schubert et al., 1999). This is clearly an undesirable feature for the forcing of a numerical model such as ours, as energy will be continually available to be fed into the unstable barotropic modes, but the concomitant horizontal mixing will not remove the source of the instability, as it would in the real atmosphere or a fuller model. Accordingly, we modify the profile inside the RMW to have a cubic dependence of V on r,

$$V(r) = c_1 r + c_2 r^2 + c_3 r^3, \qquad r < r_{\max}, \qquad (6)$$

where c_1, c_2, and c_3 are chosen to make V and its first two derivatives continuous at the RMW. A cubic dependence was chosen as this was similar to the stable profiles in Schubert et al. (1999) and was the simplest modification that had continuous radial derivatives of vorticity and inertial stability. The linear model results indicate the need for a continuously differentiable radial profile of vorticity, in that Eq. (28) of Part I shows that discontinuities here will lead to discontinuities in w, which is undesirable as it could cause numerical problems. The profile used is relatively broad at the RMW, while observed profiles are often quite sharp there. This may have a small effect on the relative jet strength very close to the RMW. However, such a profile cannot be easily tested in the present model because of the need to not allow barotropic instability.

In the cases analyzed here, the prescribed environmental flow is the same as the cyclone translation, so the gradient wind is the sum of the environment and vortex flows. This is easily shown by changing to a coordinate system moving with the vortex. The flow at the top of the model would not be expected to be exactly in gradient balance, since the dynamics there includes horizontal and vertical diffusion, and vertical advection.

The remainder of the upper boundary condition is that vertical gradients of heat, velocity and turbulent kinetic energy are zero. The asymmetric component in Part I may still have an amplitude of 1 or 2 m s^{-1} at

TABLE 1. Parameters defining the storms discussed in the text. The maximum wind is the gradient wind that would apply for a stationary asymmetric storm in the Holland (1980) parametric model. Radius of maximum winds is the radius of maximum gradient wind, and b is the parameter determining the amount of peakedess in the parametric radial wind profile. These first four parameters determine the central pressure deficit, relative to the environment.

Storm	Max wind	RMW	b	Latitude	Storm movement
I	39.3 m s^{-1}	40 km	1.3	15°N	0
II	39.2 m s^{-1}	40 km	2.1	15°N	0
III	59.2 m s^{-1}	40 km	1.3	15°N	0
IV	39.3 m s^{-1}	40 km	1.3	15°N	5 m s^{-1}

the model top, as the depth scale δ_{-1} of the dominant asymmetric component is similar to the model depth. The top boundary condition used should not interfere with the nonlinear analogue of this. To check, we performed one integration with double the domain depth, and found the results to be very similar to those obtained from our usual domain, including the representation of the asymmetric flow at these levels.

In the terrain-following coordinate system, the vertical velocity and the wind at $z^* = 0$ are equal to zero. The lower boundary condition for turbulent kinetic energy is derived by assuming balance between dissipation and production terms in the turbulent energy equation, and by applying Monin–Obukhov similarity theory.

On the lateral boundaries, a radiation boundary conditions after Orlanski (1976) is used. Sensitivity experiments showed that the results discussed in this study are little affected by the lateral boundary conditions used.

3. The boundary layer of a symmetric storm

Here we consider three stationary, symmetric storms in a quiescent environment. In the first two cases, the wind and pressure profiles are representative of a moderate cyclone with maximum gradient level wind of 39.3 m s^{-1} at a radius of 40 km. Storm I has a moderate radial wind profile and is the same as the case analyzed using the linear model, while storm II is much more peaked, giving an annulus of zero radial angular momentum (M_a) gradient outside the radius of maximum winds. Storm III is inertially stable throughout, but considerably more severe, with a maximum gradient wind of 59.2 m s^{-1}. Parameters used in defining the storms are defined in Table 1, while Fig. 1 shows their radial profiles of gradient level wind speed and absolute angular momentum.

a. The inertially stable case

A radial cross section through the inner part of storm I is shown in Fig. 2. The azimuthal flow at 2 km is very close to gradient balance, so clearly supergradient flow occurs at some height everywhere outside the RMW, and to some distance inside. It is clear also that the height of the jet decreases markedly toward the center,

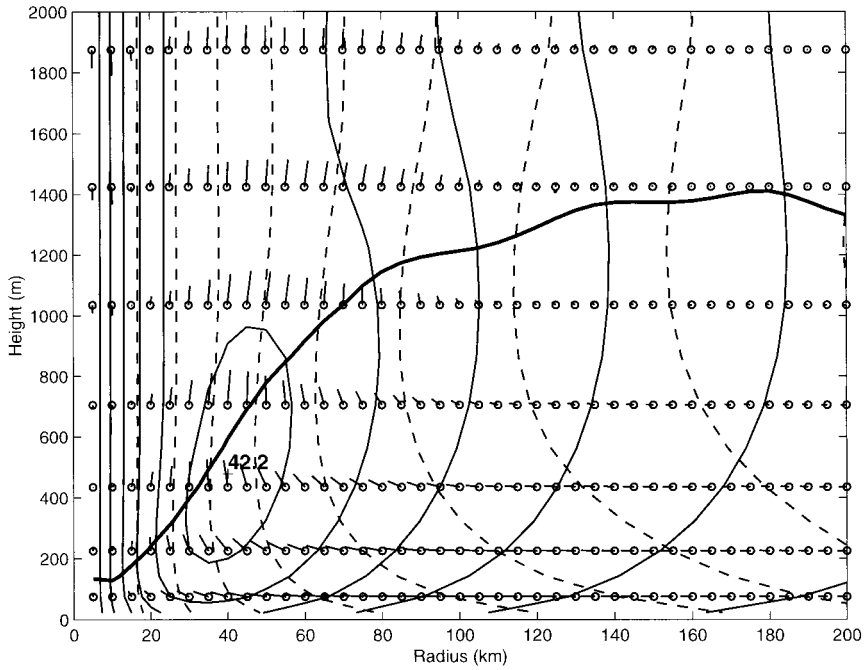

FIG. 2. Radial cross section through storm I. The solid light lines are contours of v, the dashed contours of M_a, the solid heavy line marks the top of the layer in which vertical diffusion plays a marked role in the dynamics, the vectors are of (u, w) with only every second model level shown.

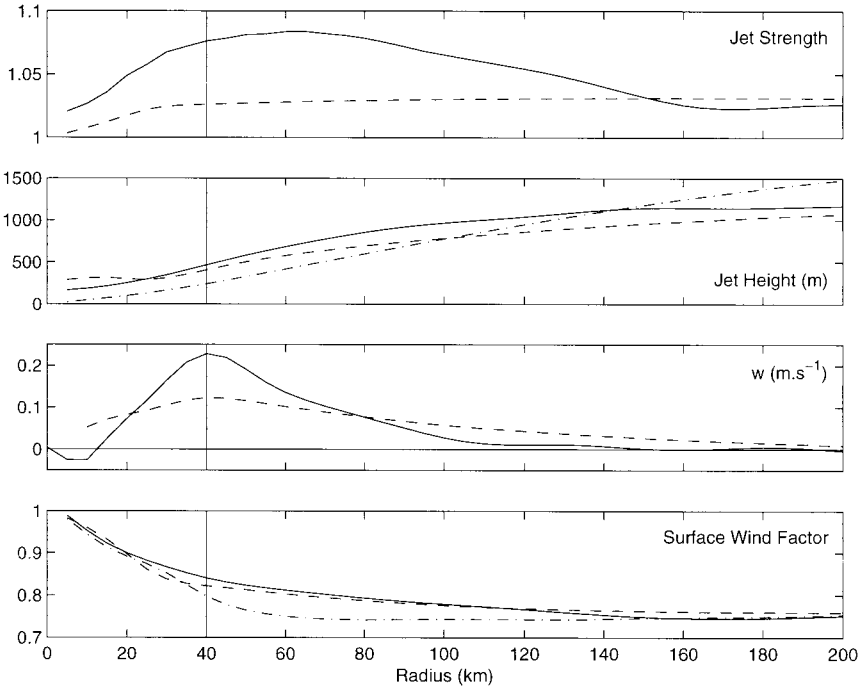

FIG. 3. A comparison of jet strength (top) and height (second from top), vertical velocity at 700 m (second from bottom), and surface wind reduction factor (bottom), between the linear (dashed lines) and numerical (solid) models, for storm I. The height panel additionally includes the variation of V/I (dash–dotted), which was proposed as a turbulence-parameter-free scale for the jet height. The wind reduction factor additionally shows a model-derived reduction from 700 m, near or below the jet height (dash–dotted). The vertical lines in each panel are at the radius of maximum winds.

in agreement with the results of the linear model. The upper panels of Fig. 3 show that the linear model performs remarkably well in predicting the jet height, but substantially underpredicts the strength, for reasons to be explored below. For this comparison, we used the drag coefficient and average turbulent diffusivity below 1 km from the full model calculation, in the linear model. This was necessary to ensure that both models represented the wind speed dependence of these parameters consistently. The choice of 1 km as an averaging height for the diffusivity was arbitrary, and other reasonable choices made only a small difference.

Also shown in Fig. 2 are contours of M_a, which bow outward above the jet as the wind speed decreases. The vectors of (u, w) follow the M_a contours above the jet, demonstrating that diffusive processes play only a very minor role here. The heavy solid line shows the height at which the advection of M_a goes to 1% of its surface value at that radius. Diffusion plays a negligible role on the budget of M_a above this, but, as we shall see shortly, is still important to the radial flow balance up to about 1 km.

The scaling V/I for jet height proposed in (I.26), also shown in Fig. 3, is seen to underestimate the height near the cyclone center. This is because in the numerical model, K increases toward the center more rapidly than the scaling (I.25), since the turbulence length scale in the closure scheme used does not diminish toward the center as δ_0 does. This in turn is because in the strong ascent at the core, there is no marked increase in static stability above what we have identified as the boundary layer top. Thus the turbulence closure is unable to identify the boundary layer top, and reduce its length scale accordingly. Clearly there is an inconsistency between our scaling arguments for K and our turbulence closure implementation; which length scale formulation is correct is less clear. If we had instead taken the turbulence length scale constant with radius in our earlier scaling argument we would have found $\delta_0 \sim (V/I)^{1/2}$ which would tend toward zero less strongly in the core than V/I, and been more consistent with the numerical model. Neither formulation is particularly inconsistent with currently accepted boundary layer theory; perhaps what this best illustrates is that the tropical cyclone boundary layer has some unusual aspects that require further research.

The extreme shallowing of the boundary layer toward the center could account for some of the large variability observed in observed wind profiles. For instance, consider two profiles taken from Fig. 2, at 24- and 69-km radius, both with a gradient wind speed of 35 m s^{-1}, but on opposite sides of the RMW. These profiles are separated by a mere 45 km, yet the jet heights differ by a factor of over 2, and the corresponding near-surface

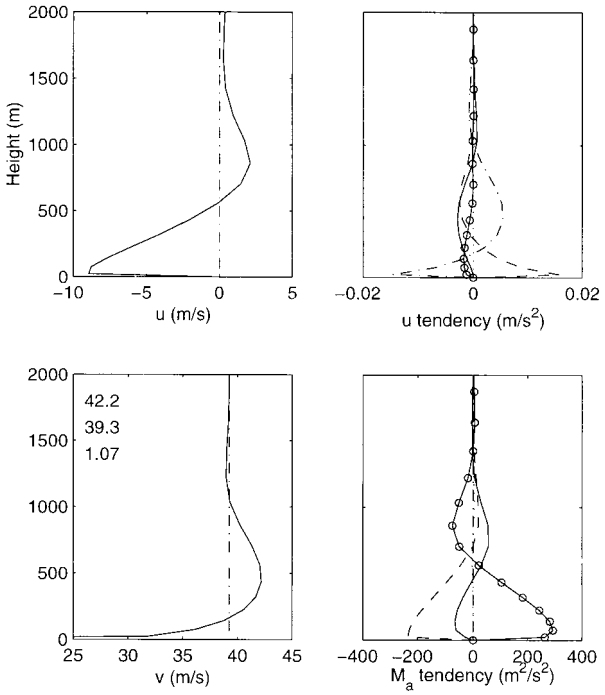

FIG. 4. Vertical profiles of radial (top left) and azimuthal (lower left) velocity components, for a point in the eyewall of storm I. The dashed lines represent the gradient wind at that point. Note the strong inflow at the surface and weak outflow above 1 km, and the broad supergradient jet maximum around 600 m. Budgets of radial velocity (top right) and angular momentum (lower right) for the same point. The components are horizontal advection (solid with circles), vertical advection (solid), vertical diffusion (dashed), horizontal diffusion (dotted), and adjustment (dash–dotted). The adjustment terms for the radial velocity represent the acceleration due to the imbalance in the pressure gradient, coriolis and centrifugal terms. For M_a, the adjustment is simply the azimuthal pressure gradient, which is zero in this axisymmetric storm. The numbers in the lower left panel are the maximum azimuthal wind, gradient wind, and their ratio, at this point.

winds are 30.4 and 27.4 m s^{-1}, respectively, giving surface wind factors of 0.87 and 0.78.

The updraft at the RMW is nearly twice as strong as in the linear model, as well as being less widely distributed (Fig. 3, 3d panel). The surface wind factor (Fig. 3, last panel) is very close to that derived using the linear model. Also shown is a surface wind factor calculated relative to the wind at 700 m, at or below the jet height, which might be expected to remove some of the increase toward the center. It is nearly constant outside the RMW, but the strong gradient inside remains.

Figure 4 shows vertical profiles of radial and azimuthal wind for a point at the RMW of storm I. Again, the flow is nearly gradient above 1 km, and it is therefore natural to identify this as the top of the boundary layer. This is a few hundred meters higher than the dark curve in Fig. 2, which was based rather on where the influence of vertical diffusion on the angular momentum budget became negligible. We will see that vertical diffusion is important to the radial flow balance up to about 1 km, so prefer to regard this as the top of the boundary layer. Below this height, the inflow component increases steadily to a maximum of 9 m s^{-1} at about 100 m, while the azimuthal component shows a broad maximum of 42.2 m s^{-1} at 500 m, which is 7% supergradient.

The terms in the balance equations for radial velocity and absolute angular momentum are also shown in Fig. 4. Looking first at the angular momentum, we see that below the jet maximum, the inward advection of angular momentum is balanced largely by vertical diffusion, with upward advection playing a smaller, also weakening role. Above the jet maximum, transport of jet momentum by the eyewall updraft becomes important. This is balanced by a weak outflow of around 1 m s^{-1}, which reverses the sign of the horizontal advection term. Note that the contribution of vertical diffusion becomes very small above 700-m height.

The budget for radial velocity at levels where the flow is supergradient is dominated by the imbalance in the gradient wind terms (i.e., the pressure gradient, coriolis and centrifugal terms). This is balanced largely by upward advection and vertical diffusion of inflow, with a smaller contribution from horizontal advection. Above the jet, the gradient wind imbalance maintains the weak outflow mentioned above—in essence, supergradient momentum carried aloft by the eyewall updraft is centrifuged out from the storm center, leading to a return to gradient balance as the influence of the frictionally forced inflow recedes. This role of ascent, in helping to define the top of the boundary layer, is in contrast to the usual role of vertical motion in boundary layer dynamics, where subsidence produces a shallower boundary layer with a more marked top, and emphasizes the strong departures we are finding from textbook ideas of one dimensional horizontally homogeneous boundary layers. Note that the model is dry and so may be underestimating the updraft strength as it does not include the buoyant forcing due to latent heat release. This would further strengthen the jet, although is probably not a major issue as the jet heights we find are near or below typical cloud bases.

Closer to the surface, the radial flow balance is almost entirely between the gradient wind terms accelerating inflow, and vertical diffusion retarding it, as in the linear model. Horizontal advection is larger here than aloft, but still dominated by the other terms.

Some of the effects of the linearization in the analytical model can also be discerned from Fig. 4. The M_a budget at and below the jet is largely a balance between radial advection of angular momentum and its turbulent transport into the sea, as required by the linear model. Vertical advection plays a significant, but generally not dominant role there, being several times smaller than and opposite in sign to the horizontal advection. Above the jet, the vertical advection of M_a dominates the vertical diffusion, but since its sign is generally the same, it does not produce qualitatively different results to the linear model. Calculating the radial advection using $\partial M_a/\partial r$ at the top of the boundary layer, as in the linear

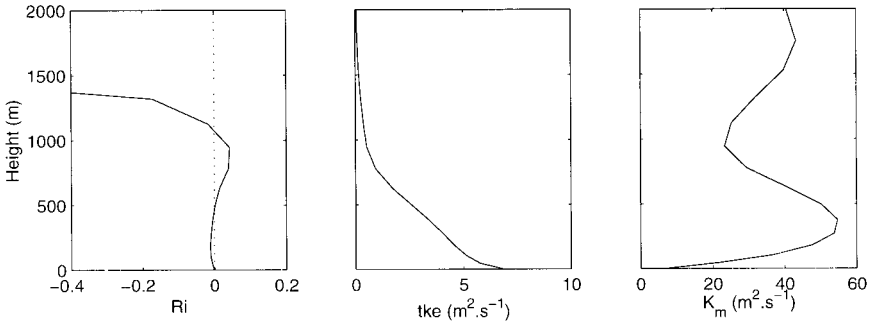

FIG. 5. Vertical profiles of Richardson number (left), turbulence kinetic energy (center) and turbulent diffusivity for momentum (right), for the same eyewall point in the same storm as Fig. 4.

model, rather than within it as here, produces its largest inaccuracies near the surface. However, as the surface wind reduction factor is around 0.8, the relative error is not large.

In contrast, vertical advection of radial velocity is of similar importance to vertical diffusive transport in the upper part of the boundary layer. It was the linear model's neglect of this which so weakened the jet there, and is thus the major shortcoming of that model. This is in accordance with the heuristic argument we advanced in Part I, and also the scaling argument of Smith (1968) cited there, but note that the stronger updraft in the nonlinear model will provide an even greater enhancement. Figure 3 contains further evidence that it is the neglect of vertical velocity which is the major reason for the weak jet in the linear model. Outside of 140 km, where the numerical model has almost no updraft, the two models agree closely on the jet strength. Inside of this, where the updraft becomes significant, the numerical model produces a much stronger jet than the linear model. Vertical advection of radial flow is of greater importance to jet development than to surface wind strength, as it tends to be is largest in the middle and upper boundary layer where w is approaching its peak and before $\partial u/\partial z$ starts to decline. Thus the neglect of vertical advection does not greatly affect the surface wind factor.

In contrast, the $u\partial u/\partial r = \partial(u^2/2)/\partial r$ term would be expected to be larger in the lower part of the boundary layer (where the inflow is stronger) and in the inner core, where inflow is beginning to decrease rapidly toward zero at the center. It may also be important beneath buoyant updrafts, where observational studies have found a marked radial gradient of inflow. It is therefore more important to the strength of the near-surface winds than to the strength of the jet, and would lead to weaker near-surface winds outside the radius of maximum inflow, and stronger ones inside, than would apply if it was omitted. Near the surface, the radius of maximum inflow is about 60 km, and we find that this term is largest in the vicinity of the RMW. However, the inflow budget there is shown in Fig. 4 to be dominated by the vertical diffusion and gradient imbalance terms, with horizontal advection being much smaller. So neglect of this term in the linear model does not produce substantial errors in the near-surface flow in this case.

Although the linear model substantially underpredicts the jet strength in regions of strong updraft, it is considerable more successful with the height. The linear model boundary layer depth scale δ_0 ignores vertical advection. However, w increases from 0 at the surface to a maximum at the boundary layer top. Adding vertical advection to the physics does not therefore introduce any fundamentally new depth scale, but rather modifies that already pertaining, and so the linear model scale for jet height is applicable here.

In summary, the analytical formulas for jet height and surface wind factor derived from the linear model are applicable to the full model, as the nonlinearities are not dominant influences to these. However, vertical advection of inflow contributes strongly to jet strength, which is substantially underpredicted by the linear model.

We now show that the jet here is distinct from the familiar nocturnal jet. The latter has been widely studied, with many simulations of data from, for example, the Wangara experiment (Clarke et al., 1971), showing the effect. Here, we shall make comparison with the simulation of Mellor and Yamada (1974, henceforth MY74) as they use a similar turbulent closure to our model, and include figures of all the relevant terms.

Figure 5 shows the Richardson number Ri, the turbulence kinetic energy (TKE), and the turbulent diffusivity for momentum for the same RMW point in storm I. We note first that Ri is very small in magnitude through the boundary layer, suggesting shear production will dominate the TKE budget, and is in fact slightly negative at and below the jet. This is completely contrary to the situation in the nocturnal jet (MY74 Fig. 5), where strong stabilization and buoyant suppression of turbulence are necessary for the decoupling, which then allows the inertial oscillation that produces the jet. The TKE decreases from a surface maximum to become nearly zero at about 1 km, the top of the boundary layer, so the jet here occurs entirely within the boundary layer. Again, this is distinct to the nocturnal jet, which occurs

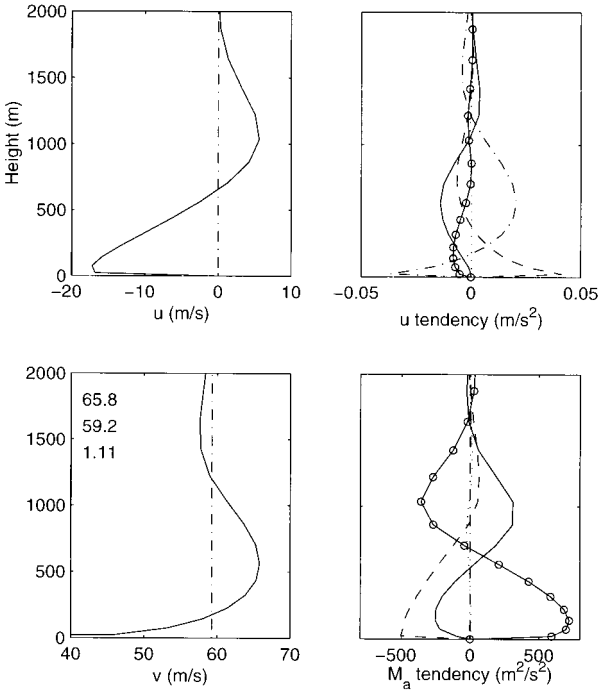

FIG. 6. The same as Fig. 4, except for a point in the eyewall of storm III.

at the top of the nocturnal boundary layer, where TKE has become essentially zero (MY74 Fig. 6). Finally, we see that the turbulent diffusivity has a maximum immediately below the jet. This maximum occurs because the diffusivity in the level 2¼ closure is the product of the square root of the TKE, the master length scale, and a stability dependent term. Their respective height variation through the boundary layer is to decrease to nearly zero, to increase from zero and to be nearly constant, with the net result being a maximum about halfway up the boundary layer. This confirms that the jet is in a region of strong turbulent transport, and is therefore not a consequence of frictional decoupling. The negative values of Ri, and local maximum in K_M, above 1500 m, are a consequence of weak static instability and weak shear well above the boundary layer in the numerical model, and are of no dynamical significance. We note, however, that Black and Holland (1995) found evidence of a jet due to surface cooling and low-level decoupling in the periphery of Tropical Cyclone Kerry (1979). The large positive values of Ri they found beneath the maximum suggest it may be distinct to the one being analyzed here.

Turning to the more intense storm III, we find that the jet is again most marked near the RMW, where at 65.8 m s^{-1} it is 11% stronger than the gradient wind. Figure 6 shows vertical profiles of angular momentum and radial velocity, as well as the terms in the budget equations. These are remarkably similar in appearance to those for the weaker storm I, albeit with considerably larger values. One significant change is that the outflow above 1 km has become considerably more marked. The strong upward advection of M_a responsible for this is partly due to the larger vertical gradient of M_a associated with the stronger jet, but more to the fact that the eyewall updraft has tripled in strength, giving much stronger vertical advection in this more intense storm. The other nonlinear term, $u\partial u/\partial r$, has also increased in relative importance here, although is still dominated by the diffusion and adjustment terms. Thus, as before, the main shortcoming of the linear model of Part I is its neglect of vertical advection.

Our analysis so far has strongly suggested that the radius of maximum winds is a highly favorable location for low-level jet occurrence, due to the sudden increase in inertial stability allowing a strong updraft there, and the increased radial gradient of M_a.[2] Tropical cyclone rainbands are also associated with strong updrafts, and observational studies (Powell 1990a) have shown that the strong convergence beneath the band is associated with enhanced inflow on the outer side of a band, and weak or absent inflow on the inward side. Also, the along-band wind maximum sometimes observed would give an enhanced radial gradient of M_a to the outside of the band. We have shown that inflow across such a gradient will generate a jet, and that an updraft will enhance it. We therefore speculate that rainbands may be a particularly favourable location for jets. We note, however, that the mechanism described here can produce supergradient flow anywhere there is inflow and inertial stability, and also that the observational record is equivocal. While Moss and Merceret (1976) found their jet in such a location, Powell's analyzed along-band flow (1990a, his Fig 13b) shows a maximum at about 500 m extending from about 5 km outside, to at least 20 km inside, of the band. Similarly, of the three-stepped descent profiles he presents (his Fig. 15), the two taken inside the band show a jet at about 500 m, while the one taken outside the band show no evidence of a jet. Clearly, the rainband-scale structure of the jet requires further research.

b. *The inertially neutral case*

The radial strength and height of the jet for the peaked wind profile, storm II, where gradient level absolute angular momentum is essentially constant with radius for several hundred kilometers outside of the radius of maximum wind, are shown in Fig. 7. With no possibility for radial advection of angular momentum outside of 60-km radius, the jet is confined to the immediate vicinity of the RMW, where the steep, almost steplike, gradient in M_a produces a marked jet with azimuthal wind component 48.1 m s^{-1}, or 22% supergradient, at 700 m, just inside the RMW. The updraft is likewise now restricted to the vicinity of the RMW, and the sur-

[2] These are of course related, through $I^2 = r^{-3}\partial M_a^2/\partial r$.

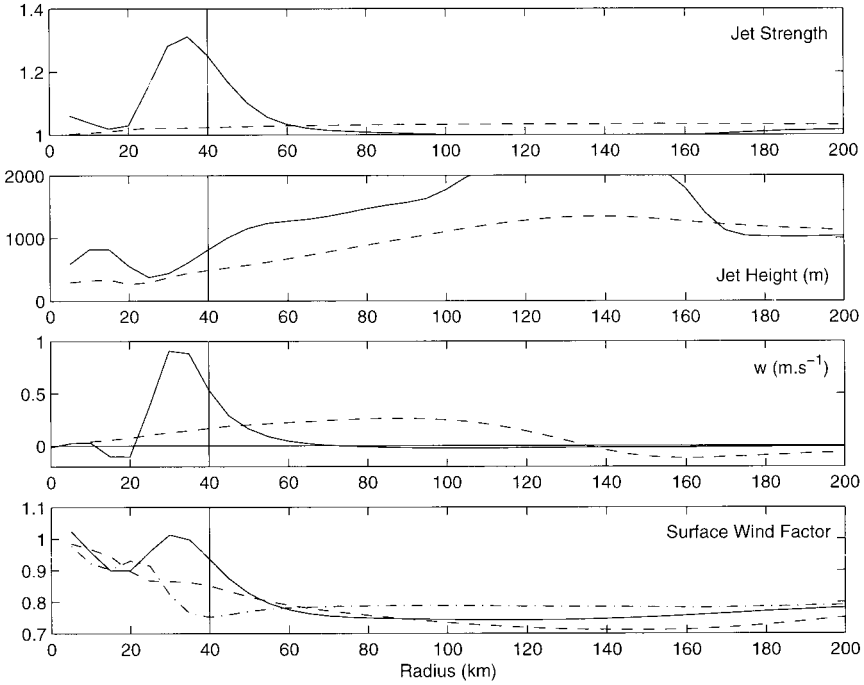

FIG. 7. The same as Fig. 3, except for storm III.

face wind factor shows a large peak here associated with the strong jet. In contrast to the previous cases, and as might have been expected from our earlier discussion, the linear model is much less successful here, being outside its range of validity through the annulus of inertial neutrality.

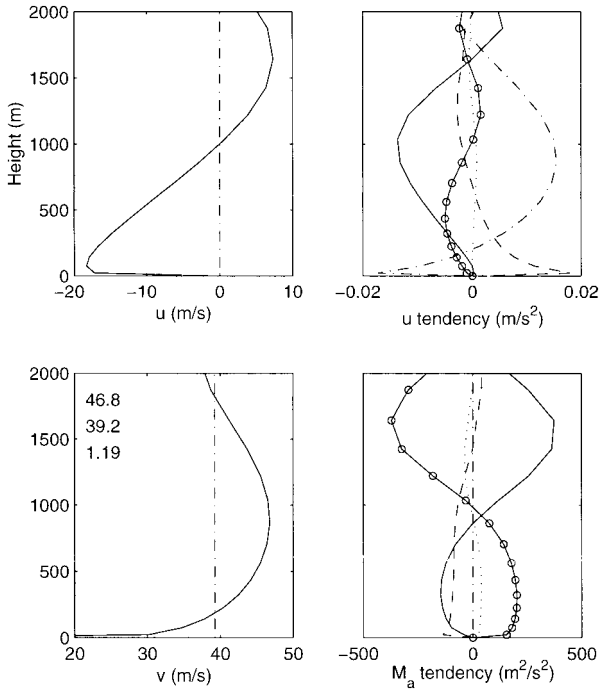

FIG. 8. The same as Fig. 4, except for a point at the radius of maximum winds for storm II.

Vertical profiles and budgets of u and M_a at the RMW for this storm are shown in Fig. 8. Although the signs of the various terms and the general shapes of their profiles are similar to those for storm I, their relative magnitudes and depth scale have changed dramatically. Both the strength of the jet and the strength of the near-surface inflow have more than doubled relative to storm I. This is accompanied by substantial increases in the contribution from nonlinear advective terms in the budgets. In particular, vertical advection is now approximately as important as vertical diffusion in balancing the inward advection of angular momentum below the jet, while above there is now substantial outflow as the strongly supergradient flow in the updraft returns to balance. In the radial flow budget, vertical diffusion is of relatively minor importance away from the surface, and the outward acceleration due to gradient adjustment is balanced largely by upward advection of inflow.

This great increase in the importance of vertical advection is largely due to the much stronger updraft in this storm. Indeed, the radial distribution of vertical velocity, shown in Fig. 7, is quite different in the two storms, with the much stronger eyewall updraft in storm III being surrounded by a ring of weak subsidence, as was hinted at in our analysis of the linear model. Since the storm is symmetric, the horizontal divergence associated with this subsidence requires that the inflow increase inward at least as rapidly as $1/r$. Thus the near-surface inflow at the RMW here is twice as strong as in storm I.

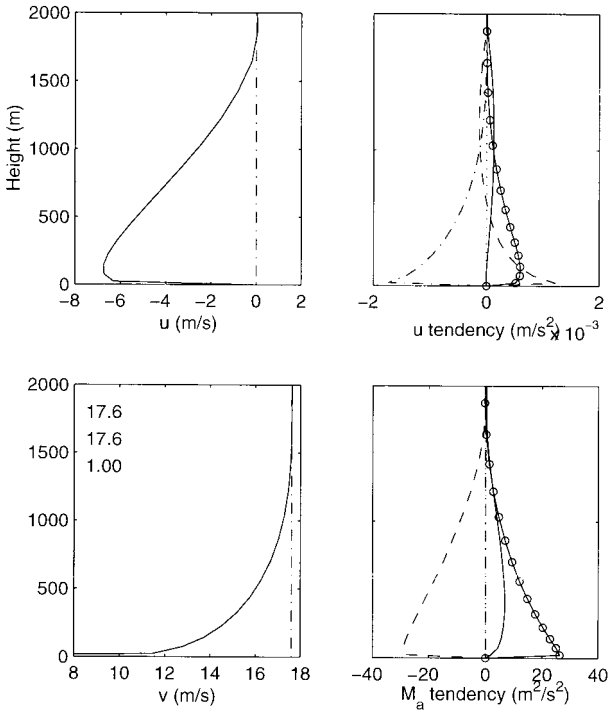

FIG. 9. The same as Fig. 4, except for a point at 3 times the radius of maximum winds for storm II.

The dynamics behind this rapidly accelerating inflow are shown in Fig. 9, which shows wind components and budgets at 3 times the RMW, near the peak subsidence. Frictional destruction of M_a near the surface produces subgradient flow there, and consequently a strong inward acceleration in the adjustment term in the radial wind budget. Except very near the surface, this inward acceleration is balanced dominantly by the $u\partial u/\partial r$ term rather than by friction. From a Lagrangian point of view, the imbalance in the adjustment terms directly accelerates the air parcels inward. In the inertially stable storm, the inflow produced sufficient horizontal advection of M_a to balance the frictional destruction. While storm II here has zero radial gradient of M_a at gradient level, the lighter winds near the surface increase the relative importance of the $fr^2/2$ term over rv and allow a weak near-surface radial gradient of M_a. The accelerating inflow thus provides sufficient radial advection of M_a to largely balance frictional destruction. Downward advection by the subsidence makes a further contribution, which is of similar magnitude to horizontal advection above 1 km.

In summary, frictional destruction of M_a outside the RMW produces inflow. In this storm, only weak advection of M_a then arises, so the inflow continues to accelerate, leading to low-level divergence and subsidence. When the inrushing air encounters the inertially stable core, overshoot (shown by the $u\partial u/\partial r$ term in Fig. 8) leads to a very strong jet and near-surface winds. Gradient adjustment of these strong winds eventually stops the inflow, with a strong updraft resulting.

The much stronger inflow in this case can be related to the results of the balanced vortex diagnostic models (e.g., Willoughby 1979). A key finding of these was that the strength of the radial response to forcing in an axisymmetric tropical cyclone was determined by the inertial stability. Our much stronger inflow in the inertially neutral storm II can be regarded as a consequence of this. Note, however, that the balanced models do not produce supergradient flow since they are by definition balanced, and that where they produce outflow above a layer of boundary layer inflow, it is because their high background static stability vertically constrains a circulation whose outward branch's role is to satisfy continuity. In contrast, the outflow above the jet found here is a direct result of gradient imbalance. Our boundary conditions impose no stability constraint on upward motion above the boundary layer, and we allow mass to exit the top of the model. We feel this is appropriate, since is a real cyclone latent heat release would be occurring in this updraft, and while the balanced vortex modelers have been concerned with the cyclone-scale response to various forcings, we are instead concerned with the boundary layer response to forcing by the cyclone.

In summary, this storm is quite different to the inertially stable case, in that nonlinear processes completely dominate those in the linear model. The poor comparison between the models in Fig. 7 is thus not surprising.

4. The effect of cyclone movement

We now consider storm IV, which is identical to storm I, but embedded in and translating with a 5 m s^{-1} easterly flow. It thus corresponds to the moving storm case considered in Part I.

The near-surface storm-relative wind field for this storm is shown in Fig. 10. The maximum azimuthal wind is located in the left forward quadrant, with the strongest winds just inside the radius of maximum gradient level winds. This is downstream of the maximum storm-relative inflow, in the right forward quadrant. The maximum earth-relative azimuthal and inflow components (not shown) lie in the right forward and right rear, quadrants, respectively. This distribution is highly consistent with the linear model, as well as the observational studies cited earlier.

The vertical velocity is strongest in the right forward quadrant, with weak subsidence opposite, in good agreement with the linear model. However the asymmetries are markedly stronger, and located closer to the RMW, than before, while the anticyclonic spiral character of w is more marked. The sense of this spiral is opposite to that for a rainband, and it is confined to the vicinity of the RMW. Thus it should not be interpreted as a forcing for a rainband, but rather an eyewall asymmetry

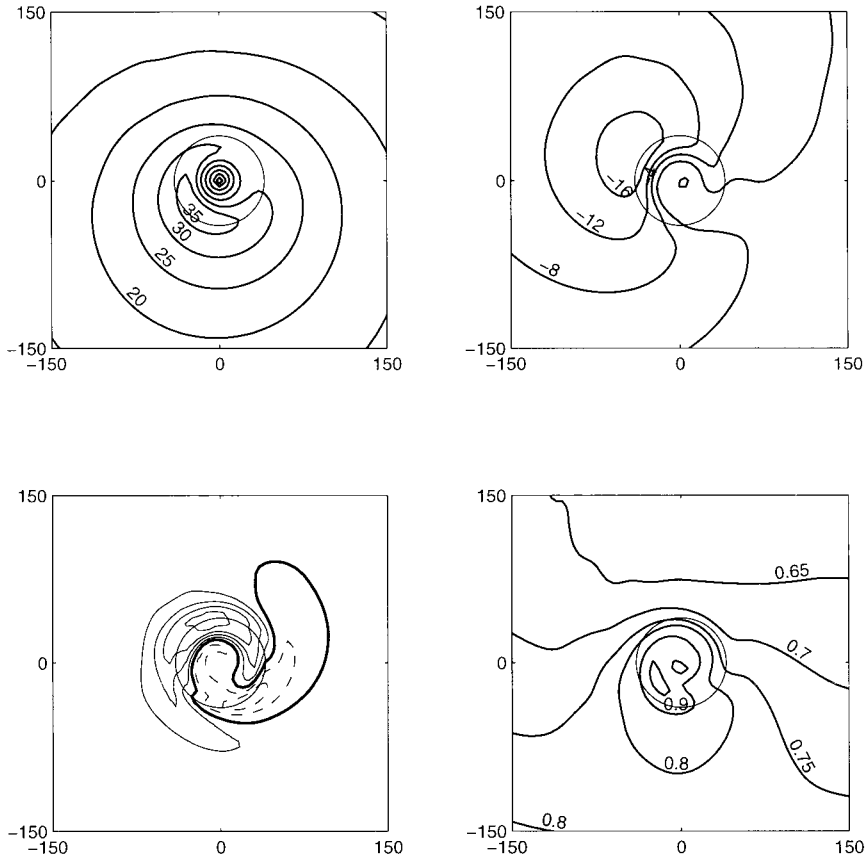

FIG. 10. Storm-relative azimuthal (top left) and radial (top right) flow, at 22 m, for storm IV; that is, the same cyclone as in Fig. 2, except moving to the left at 5 m s^{-1}. Vertical velocity (lower left) at 2 km for the same storm (zero contour heavy, negative contours dashed, contour interval 0.2 m s^{-1}). Wind reduction factor from the gradient wind to 22 m for the same storm (lower right), in stationary coordinates. The light circles in each panel indicate the position of the radius of maximum winds.

similar to that in the (u_{-1}, v_{-1}) component of the linear model. The surface wind factor is in close agreement, although a little weaker, than was found in the linear model.

The distribution and relative magnitude of the jet is shown in Fig. 11. The virtual obliteration of the jet to the right rear of the storm is in very good agreement with the linear model. However, the structure to the left front of the storm is rather different. The strongest jet is in the left forward quadrant just inside the radius of

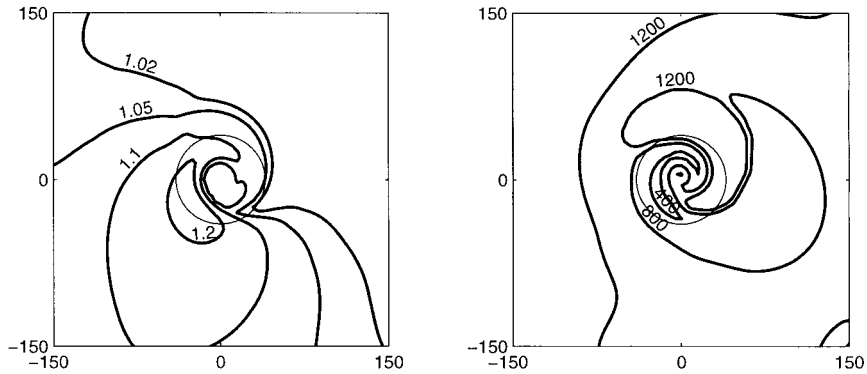

FIG. 11. Jet strength (left; relative to the gradient wind speed) and height (right) for the leftward moving storm IV.

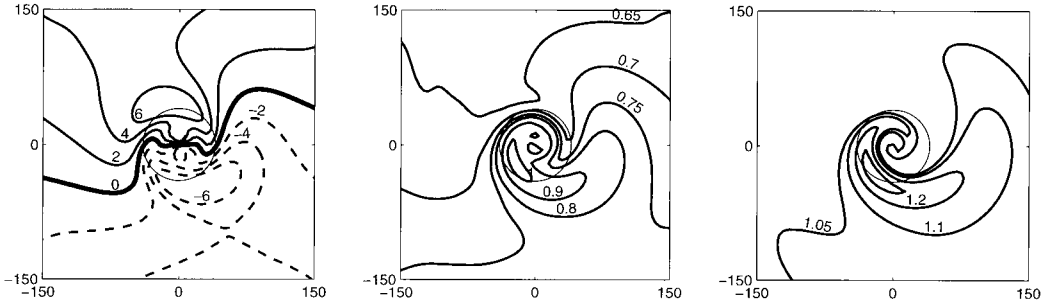

FIG. 12. The asymmetric component of the azimuthal flow in stationary coordinates at 1.875 km (left), and the surface wind reduction factor (middle) and jet strength (right) relative to the 1.875-km wind speed, for storm IV.

maximum gradient winds, where it is 29% supergradient, or roughly 4 times what was found in the stationary nonlinear case. This large value will be shown to be partly due to the conjunction of some favorable nonlinear factors, combined with the basic asymmetry described by the linear model. Our maximum jet location is slightly downwind of where Shapiro (1983) found the maximum winds (which were also supergradient) in his slab model, although some care is needed in comparing our maximum wind within a profile, with Shapiro's mean wind in a slab boundary layer. There is a steep radial gradient of jet height around here, but the height of the maximum jet is 450 m.

A subtlety arises in calculating the jet strength and surface wind factors. So far, we have presented these relative to the gradient wind, in earth-relative coordinates. However, in practice, the gradient wind is hard to measure and it might be preferred to use, for instance, an aircraft measurement at 2-km altitude. For the stationary storm, the boundary layer is shallow and there is no practical difference. However, the components (u_{-1}, v_{-1}) in the linear model had a distinctly larger depth scale, and examination of the flow near 2 km in the numerical model shows a similar but much larger wavenumber 1 asymmetry, of amplitude ± 6 m s^{-1} (in stationary coordinates). This is large enough to have a significant effect on the patterns of surface wind factor and jet strength if they are calculated relative to this, rather than to the gradient wind. Figure 12 shows the asymmetric earth-relative azimuthal flow at 1.875 km from the numerical model, and the surface wind factor and jet strength calculated relative to the total wind (in stationary coordinates) at this level, which should be compared to those in Fig. 11. The latter two fields show an area of enhanced values extending into the right rear quadrant, precisely where the asymmetric v component is acting to reduce the net 1.875-km azimuthal component. Comparison on this basis also reduces the apparent strength of the surface and jet flows in the left forward quadrant, where the asymmetric v component increases the 1.875-km wind. This suggests that for practical use, different factors may be required depending upon whether one is trying to reduce gradient winds, or observations, to the surface.

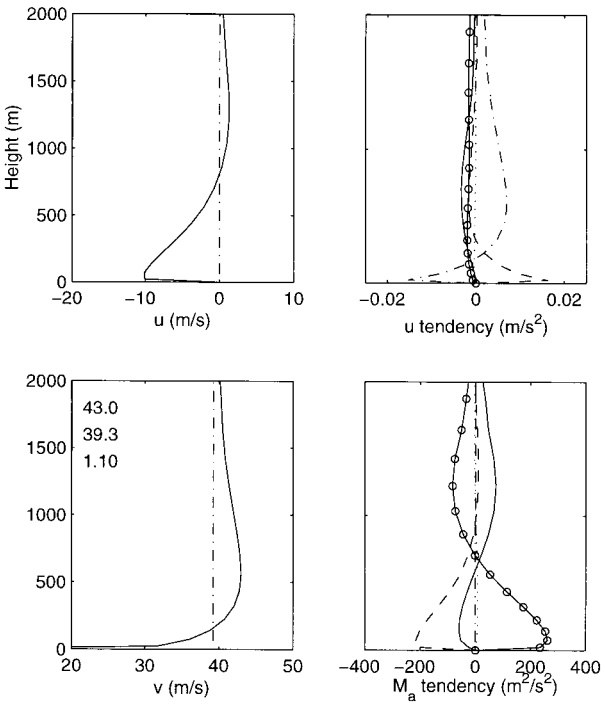

FIG. 13. The same as Fig. 4, except for an azimuthal average around the radius of maximum winds in storm IV.

In the linear model, the flow components due to the motion were independent of the symmetric component. While we would expect interaction between these components in a full model, the symmetric part nevertheless provides a good starting point for understanding the flow here. The azimuthal average around the RMW of the wind components and their budgets is shown in Fig. 13. The strength of the jet and near-surface inflow have both increased by less than 1 m s^{-1} from the stationary case, while the mean updraft at 1 km (not shown) has gone from 0.22 m s^{-1} to 0.32 m s^{-1}. Similarly, the jet height, and terms in the momentum budgets, are in very good agreement with the stationary case. The major difference is that the supergradient flow extends much higher than in the stationary case. However, our overall picture

of vertical advection and turbulent transport of inflow being necessary to maintain the inflow against gradient adjustment of the supergradient jet is still valid.

The asymmetries in the jet can be understood either in terms of the linear model, or in terms of enhanced inflow forcing (associated with storm asymmetries) allowing stronger supergradient flow to develop. Here, we give both interpretations. At the RMW at the front of the storm (Fig. 14a), low-level inflow is maintained in the presence of a 22% supergradient flow by both horizontal and vertical advection. The role of vertical diffusion, in contrast to the stationary case, is virtually negligible here. The horizontal advection is dominated by the azimuthal advection of the asymmetric part of u (not shown), a term which is included (in linearized form) in the linear model. The inflow layer is about 1 km deep, the substantial outflow aloft being associated with a sign reversal of the angular momentum advection term and a gradual return to gradient balance above the jet. A comparison of the symmetric and full components of the radial wind shows that the inflow is stronger below, and the outflow stronger aloft, than in the azimuthal average. The azimuthal component here is almost everywhere stronger than its azimuthal average. Both of these are qualitatively consistent with the flow components (u_{-1}, v_{-1}) for the linear model shown in Fig. 3 of Part I.

To the left of the storm (Fig. 14b), the jet is lower, and slightly weaker. Inflow is nearly nonexistent. Here, the decline in the updraft, and also the reversal of the sign of the advection of radial flow aloft, have allowed the flow above 1 km to become subgradient. The supergradient flow closer to the surface is maintained by azimuthal advection around from the front of the storm, rather than by inward advection. The jet is thus weakening here, and may be regarded as the decaying remnants of the maximum jet found in the left front quadrant. Again, the differences between the flow here and the azimuthal average are in qualitative agreement with the linear model.

Behind the storm (Fig. 14c), no obvious jet is present below 2 km and the flow below 1200 m is both subgradient and inward, with the reverse applying aloft. The weak inflow, and azimuthal advection, both contribute to maintaining the azimuthal flow against frictional dissipation, but are insufficient to generate supergradient flow below 1 km. Only aloft is this marginally present. The flow relative to the symmetric components is now virtually reversed from that in front of the storm, and is therefore again in agreement with that found in the linear model.

Finally, to the right of the storm (Fig. 14d) the flow is broadly supergradient from 400 m to above 2 km, accompanied by strong inflow. In one sense, this flow, although supergradient, is not sufficiently confined in the vertical to be regarded as a jet. Here, the asymmetric components are quite close to being the opposite of those to the left of the storm, and thus detract from, rather than sharpening, the low-level maximum in the symmetric component. Remarkably, the terms in the angular momentum budget virtually vanish above 800 m. However, this is a somewhat misleading picture, as the radial and azimuthal components of the horizontal advection (not shown) are both of order 100 $m^2\ s^{-2}$, and cancel. This could be regarded as a characteristic of the inertial wave discussed in Part I; however, we prefer to interpret it in terms of the linear model, as an area where the peaks and troughs in the symmetric and asymmetric components cancel, as therefore do the various terms in the budgets, giving the apparently zero tendency terms above about 800 m.

It is clear from Fig. 14 that the asymmetric components of the flow are generally greater than the symmetric part near 2 km. This is consistent with the linear model, as the depth scale δ_{-1} of the dominant asymmetric component is almost twice that for the symmetric component, δ_0.

5. Summary and conclusions

Two models of the tropical cyclone boundary layer were presented and used to diagnose the properties of, and deduce the dynamics causing, the low-level jet that has been observed in the boundary layer of tropical cyclones. Each diagnoses the boundary layer flow as the frictional response to an imposed, prescribed gradient flow characteristic of a cyclone, ignoring the feedback from boundary layer processes onto the cyclone as a whole, and thus represent one side of what is undoubtedly a two-way interaction. The first, presented in Part I, is a linear analytical model which bears some resemblance to the well-known Ekman boundary layer model. However, the solution has three components, a symmetric one due to the cyclone, and two asymmetric ones resulting from the interaction of the moving cyclone with the underlying surface. Each has a different depth scale, which are each different to that of the classical Ekman solution. There is also an asymmetry between the radial and azimuthal components of the flow not present in the classic solution, which makes the radial component relatively stronger than the azimuthal in all three components.

Our second tool, a very high resolution numerical model, with a sophisticated turbulence closure and surface layer parameterization, was presented here and used to extend the analysis of Part I to include the important nonlinear terms. It was found in Part I that a supergradient jet could be produced by strong inward advection of angular momentum, with the inflow maintained against gradient adjustment by upward diffusion. However, including the nonlinear terms and particularly the vertical advection of radial wind provided enhanced inflow forcing and allows a jet that is several times more supergradient than in the linear model, and therefore more realistic. In particular, the wind maxima were found here to be between 10% and 25% supergradient

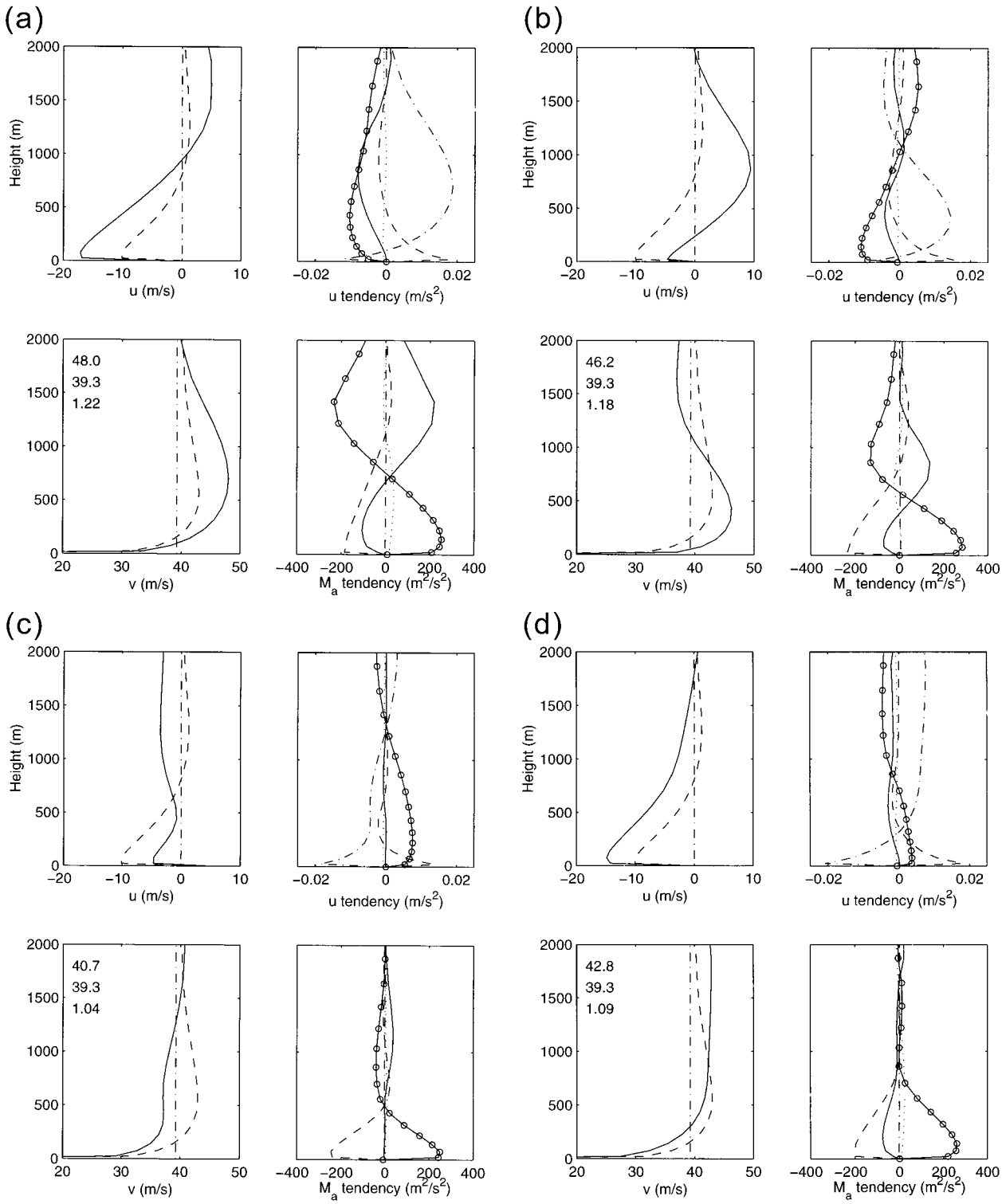

FIG. 14. The same as Fig. 4, except for four points in the eyewall of storm IV. They are (a) at the front, (b) to the left, (c) behind and (d) to the right of the storm. Flow given, and terms in the budgets, are in a coordinate system moving with the cyclone.

in a stationary cyclone, with the jet being more supergradient in a more intense system, or near the RMW in a storm with a peaked radial wind profile.

The linear model did, however, predict a jet height in close agreement with that obtained from the numerical model, especially in the inertially stable case. This seems to be because the height scale set by the turbulent diffusivity and inertial stability, $\delta_0 = (2K/I)^{1/2}$, also defines the height at which the frictionally induced updraft becomes fully established. Thus the introduction of vertical advection to the linear model does not bring any new height scales, but instead is governed by an already existing one.

Is the jet, then, nothing more than the weakly supergradient flow found near the top of the Ekman boundary layer? In Part I, it was argued that the answer is essentially yes; albeit with the complication of three separate components in a moving storm, and several reasons were given for such dynamics being more realistic in the tropical cyclone boundary layer than elsewhere in the atmosphere. In particular, the linear model of Part I used a slip surface boundary condition, buoyant generation of turbulence would be expected to be minor in a tropical cyclone boundary layer, and baroclinicity is weak. However, we showed here that vertical advection plays a crucial role in strengthening the jet, giving a supergradient component several times stronger than in the linear model. The major role of upward advection may well be peculiar to intense vortices and does not occur in more normally considered cases. This is because the rapid, almost steplike increase in inertial stability near the radius of maximum winds produces an updraft that is much stronger than would be expected from the classical theory, in which the updraft is proportional to the curl of the surface stress. We thus qualify the answer to this question given in Part I, by adding that nonlinearities significantly modify the Ekman profiles, giving markedly stronger agradient flow in the upper part of the spiral.

The spatial distribution of the jet in the axisymmetric storm was found to depend upon the peakedness of the radial gradient level wind profile. A compact storm with a relatively rapid decrease in wind speed outside the radius of maximum wind tended to produce a jet confined to the immediate vicinity of the eyewall, while a more inertially stable radial profile resulted in a more widely distributed, but less intense, jet. The difference was explained in terms of the different angular momentum profiles of the two storms, and the consequently differing abilities of the two storms to generate significant horizontal advection of angular momentum.

For a moving storm, it was found that the jet was generally located in the left forward quadrant of the storm in the Northern Hemisphere, away from the strongest earth-relative near-surface winds in the right forward quadrant. The asymmetric part of the flow was found to decay more slowly with height than the symmetric, in agreement with the results of Part I.

Surface wind reduction factors were calculated and the largest values were found to be near the radius of maximum winds, and to the left of the storm (Northern Hemisphere). Their distribution is thus similar to that of the jet. It was shown that some caution may be necessary in choosing a level for comparison in calculating these, as the asymmetric component can still be large as high as 2 km above the surface in the nonlinear model.

The use of a universal constant for surface wind reduction is thus shown by both the linear and numerical models to be incorrect. In one sense, this is hardly surprising as the strong contribution of horizontal advection to the momentum budgets means that the assumption of one-dimensionality in profile models is invalid. The variability in the reduction factor between different observational studies is similar to that found here. Since the factor most commonly called upon to explain these observed differences, namely, differences in the static stability, is not present here, we suggest that these dynamical factors are the primary cause of the observed variability.

The observational database of low-level wind profiles in the tropical cyclone core region is very small, although the recent advent of the high-resolution global positioning system (GPS) dropsonde (Hock and Franklin 1999), the Aerosonde (Holland et al. 1992), and our tower instrumentation project at North West Cape, Australia (Kepert and Holland 1997), will no doubt change this over the next few years. At present, the best we can say is that the magnitude and height of our jet is quite consistent with the few observations available. However, it appears that the GPS dropsonde in particular will be a valuable tool for testing the predictions herein of the characteristics of the tropical cyclone low-level jet, and particularly its spatial distribution.

Acknowledgments. This work was partially supported by the U.S. Office of Naval Research under Grant N-0014-94-1-0493 and forms part of the Australian Tropical Cyclones Coastal Impacts Project. Thanks are due to Mike Montgomery and an anonymous reviewer for their thorough and helpful reviews.

REFERENCES

Barnes, G. M., and M. D. Powell, 1995: Evolution of the inflow boundary layer of Hurricane Gilbert (1988). *Mon. Wea. Rev.,* **123,** 2348–2368.

Black, P. G., and G. J. Holland, 1995: The boundary layer of tropical cyclone Kerry (1979). *Mon. Wea. Rev.,* **123,** 2007–2028.

——, ——, and V. Pudov, 1993: Observations of air–sea temperature difference in tropical cyclones as a function of wind speed. *Extended Abstracts, Fifth BMRC Modelling Workshop: Parameterisation of Physical Processes,* Melbourne, Australia, Bureau of Meteorology Research Centre, 87–88. [Available as Res. Rep. 46 from Bureau of Meteorology Research Centre, GPO Box 1289K, Melbourne, Victoria 3001, Australia.]

Charnock, H., 1955: Wind stress on a water surface. *Quart. J. Roy. Meteor. Soc.,* **81,** 443–447.

Cione, J. J., P. J. Black, and S. H. Huston, 2000: Surface observations in the hurricane environment. *Mon. Wea. Rev.*, **128,** 1550–1561.

Clarke, R. H., A. J. Dyer, R. R. Brook, D. G. Reid, and A. J. Troup, 1971: The Wangara experiment: Boundary layer data. Tech. Paper 19, CSIRO Atmospheric Research, Aspendale, Australia. 362 pp.

Fairall, C. W., E. F. Bradley, D. P. Rogers, J. B. Edson, and G. S. Young, 1996: Bulk parameterisation of air–sea fluxes for Tropical Ocean–Global Atmosphere Coupled Ocean Atmosphere Response Experiment. *J. Geophys. Res.*, **101** (C), 3747–3764.

Galperin, B., L. H. Kantha, S. Hassid, and A. Rosati, 1988: A quasi-equilibrium turbulent energy model for geophysical flows. *J. Atmos. Sci.*, **45,** 55–62.

Gerrity, J. P., T. L. Black, and R. E. Treadon, 1994: The numerical solution of the Mellor–Yamada level 2.5 turbulent kinetic energy equation in the Eta model. *Mon. Wea. Rev.*, **122,** 1640–1646.

Grell, G. A., J. Dudhia, and D. R. Stauffer, 1994: A description of the Fifth-Generation Penn State/NCAR Mesoscale Model (MM5). NCAR/TN-398+STR, National Center for Atmospheric Research, Boulder, CO, 107 pp.

Helfand, H. M., and J. C. LaBraga, 1988: Design of a nonsingular level 2.5 second order closure model for the prediction of atmospheric turbulence. *J. Atmos. Sci.*, **45,** 113–132.

Hock, T. F., and J. L. Franklin, 1999: The NCAR GPS dropwindsonde. *Bull. Amer. Meteor. Soc.*, **80,** 407–420.

Holland, G. J., 1980: An analytic model of the wind and pressure profiles in hurricanes. *Mon. Wea. Rev.*, **108,** 1212–1218.

——, T. McGeer, and H. Youngren, 1992: Autonomous aerosondes for economical atmospheric soundings anywhere on the globe. *Bull. Amer. Meteor. Soc.*, **73,** 1987–1998.

Kalnay, E., and M. Kanamitsu, 1988: Time schemes for strongly nonlinear damping equations. *Mon. Wea. Rev.*, **116,** 1945–1958.

Kepert, J. D., 2001: The dynamics of boundary layer jets within the tropical cyclone core. Part I: Linear theory. *J. Atmos. Sci.*, **58,** 2469–2484.

——, and G. J. Holland, 1997: The North West Cape tropical cyclone boundary layer monitoring station. Preprints, *22d Conf. on Hurricanes and Tropical Meteorology*, Fort Collins, CO, Amer. Meteor. Soc., 82–83.

Korolev, V. S., S. A. Petrichenko, and V. D. Pudov, 1990: Heat and moisture exchange between the ocean and atmosphere in tropical storms Tess and Skip. *Meteor. Gidrol.*, **2,** 108–111. (English translation in *Sov. Meteor. Hydrol.*, **2,** 92–94).

Liu, W. T., K. B. Katsaros, and J. A. Businger, 1979: Bulk parameterization of the air–sea exchanges of heat and water vapor including the molecular constraints at the interface. *J. Atmos. Sci.*, **36,** 1722–1735.

Mellor, G. L., and T. Yamada, 1974: A heirarchy of turbulent closure models for planetary boundary layers. *J. Atmos. Sci.*, **31,** 1791–1806.

Moss, M. S., and F. J. Merceret, 1976: A note on several low-level features of Hurricane Eloise (1975). *Mon. Wea. Rev.*, **104,** 967–971.

Orlanski, I., 1976: A simple boundary condition for unbounded hyperbolic flows. *J. Comput. Phys.*, **21,** 251–269.

Powell, M. D., 1990a: Boundary layer structure and dynamics in outer hurricane rainbands. Part I: Mesoscale rainfall and kinematic structure. *Mon. Wea. Rev.*, **118,** 891–917.

——, 1990b: Boundary layer structure and dynamics in outer hurricane rainbands. Part I: Downdraft modification and mixed layer recovery. *Mon. Wea. Rev.*, **118,** 918–938.

Schubert, W. H., M. T. Montgomery, R. K. Taft, T. A. Guinn, S. R. Fulton, P. Kossin, and J. P. Edwards, 1999: Polygonal eyewalls, asymmetric eye contraction, and potential vorticity mixing in hurricanes. *J. Atmos. Sci.*, **56,** 1197–1223.

Shapiro, L. J., 1983: The asymmetric boundary layer under a translating hurricane. *J. Atmos. Sci.*, **40,** 1984–1998.

Smagorinsky, J., S. Manabe, and J. L. Holloway Jr., 1965: Numerical results from a nine-level general circulation model of the atmosphere. *Mon. Wea. Rev.*, **93,** 727–768.

Smith, R. K., 1968: The surface boundary layer of a hurricane. *Tellus*, **20,** 473–483.

Smith, S. D., 1988: Coefficients for sea surface wind stress, heat flux, and wind profiles as a function of wind speed and temperature. *J. Geophys. Res.*, **93,** 15 467–15 472.

Wang, Y., 1996: On the forward-in-time upstream advection scheme for non-uniform and time-dependent flow. *Meteor. Atmos. Phys.*, **61,** 27–38.

——, 1998: On the bogussing of tropical cyclones in numerical models: The influence of vertical structure. *Meteor. Atmos. Phys.*, **65,** 153–170.

Willoughby, H. E., 1979: Forced secondary circulations in hurricanes. *J. Geophys. Res.*, **84** (C), 3173–3183.